


ORIGINAL ARTICLE

Thermal Performance and Melting Behavior of Partially Funnel-Shaped Anisotropic Copper Foam/Paraffin PCM Within an LHTES

Masoud Mozaffari¹ | Khalil Hajlaoui² | Obai Younis³ | Awadallah Ahmed⁴ | Dana Mohammad Khidhir⁵ | Ahmad Hajar⁶ | Mehdi Ghalambaz⁷  | Nashmi H. Alrasheedi²

¹Artificial Intelligence and Simulations Research Group, SimoAI OU, Tallinn, Estonia | ²College of Engineering, Imam Mohammad Ibn Saud Islamic University (IMSIU), Riyadh, Kingdom of Saudi Arabia | ³Department of Mechanical Engineering, College of Engineering in Wadi Alldawasir, Prince Sattam Bin Abdulaziz University, Al-Kharj, Saudi Arabia | ⁴Department of Mechanical Engineering, Faculty of Engineering, University of Nile Valley, Khartoum, Sudan | ⁵Department of Petroleum Engineering, College of Engineering, Knowledge University, Erbil, Iraq | ⁶Center for Environmental Intelligence and College of Engineering and Computer Science, VinUniversity, Hanoi, Viet Nam | ⁷Department of Mathematical Sciences, Saveetha School of Engineering, SIMATS, Chennai, India

Correspondence: Mehdi Ghalambaz (ghalambaz.mehdi@gmail.com)

Received: 12 March 2025 | **Revised:** 16 April 2025 | **Accepted:** 3 May 2025

Funding: This work was supported and funded by the Deanship of Scientific Research at Imam Mohammad Ibn Saud Islamic University (IMSIU) (grant number IMSIU-DDRSP2503).

Keywords: anisotropic metal foam layer | anisotropic metal foams | copper metal foam | funnel-shaped geometry | latent heat thermal energy storage | phase change

ABSTRACT

Improving the thermal properties of phase change materials is essential for enhancing thermal energy storage systems. This paper seeks to enhance the thermal efficiency of latent heat thermal energy storage by the integration of anisotropic metal foams (AMFs). The thermal efficiency and melting behavior of partly AMF designs, with systematic variations in placement, covering, and orientation, are computationally modeled and studied to maximize heat absorption and distribution within the system. A total of 12 distinct examples were examined based on the form and proportions of a funnel-shaped anisotropic metal foam layer (AMFL) that covers between 36% and 60% of the unit. The finite element method is utilized to solve the governing equations of the system. The numerical results indicated that the geometric orientation and dimensions of the AMFL influenced the thermal performance of the system. It was observed that positioning the big AMFL nearer to the hot wall increased the melting rate by 4.9%, 5.1%, and 3.9% when the AMFL fills 36%, 44%, and 52% of the cavity, respectively. Increasing the AMFL size from 36% to 60% of the unit size for the same design led to a 3.1% enhancement in the melting rate.

1 | Introduction

Challenges to energy sustainability have arisen due to the markedly decreasing rate of finite fossil fuel resources, in addition to their detrimental environmental impacts. Incorporating phase change materials (PCMs) enables latent heat thermal energy storage (LHTES) systems to mitigate the mismatch in timing between solar energy availability and energy

requirements [1–3]. PCMs provide several remarkable benefits. They can store a significant amount of energy as latent heat while requiring minimal space. Additionally, PCMs exhibit outstanding long-term stability, ensuring both mechanical integrity and chemical reliability during repeated charging and discharging cycles. Moreover, their energy storage capacity surpasses that of sensible heat storage by a factor of 4–15 [4]. Nevertheless, these materials frequently experience slow

charging and discharging performances despite their numerous benefits due to their minimal thermal conductivity. Innovative control techniques are necessary to improve the performance of TES systems by accelerating phase change properties and enhancing heat transfer in PCMs. This objective is essential and necessitates innovative strategies to resolve this obstacle effectively. A widely adopted method for addressing this challenge involves the use of a durable and efficient enclosure, specifically designed to facilitate thermal energy exchange with the heat transfer fluid (HTF). Furthermore, PCM's effective thermal conductivity is improved through the implementation of thermal enhancement techniques, including fins [5–10], nanoadditives [11–15], and metal foams (MFs) [16–19].

Various research studies have focused on improving the thermal performance of LHTES systems by employing innovative materials and configurations. Research has explored the use of PCM combined with MF to optimize heat transfer, reduce melting times, and increase overall system efficiency. Both numerical and experimental analyses reveal how different material arrangements and thermal conditions affect energy storage and transfer performance. Awasthi et al. [20], for instance, explored the effects of paraffin and copper foam with varying porosities in shell and tube latent thermal energy storage (LTES), while other researchers examined different arrangements of PCM and MF to optimize heat transmission and melting rates. In particular, these investigations have provided valuable insights into the impact of material composition and distribution on system efficiency. They investigated the thermal performance of shell and tube LTES placed in a horizontal position filled with paraffin and two cascaded layers with different porosities and designs of CuMF. Their central finding is that there is no guarantee that the two-layer system with different porosities will always obtain the least melting time compared with the uniform system. In a related study [21], the melting process of PCM in an inclined compound enclosure partially filled with a porous medium was analyzed using a deformed mesh method, showing a notable improvement in melting rate by optimizing the porous layer thickness and inclination angle. A further study [22] on non-Newtonian PCM in a cylindrical enclosure with MF layers highlighted that porous media notably accelerate the melting process, particularly under strong nonlinear thermal conditions.

Recent numerical studies have extensively explored various enhancement strategies, including MF configurations, porosity gradients, multiple PCMs, and nanoadditives, to improve the thermal performance of LHTES systems. NematpourKeshteli et al. [23] numerically studied the thermal performance enhancement of PCM-based TES systems in a flat plate solar collector and a lobed triplex-tube heat exchanger. The study showed that the heat transfer was improved using MF, nanoparticles, and extended fins, achieving a maximum melting time reduction of 85.16% with foam and nanoparticles. In [24], a lobed triplex-tube system with Y-shaped fins, MF, and nanoparticles was optimized, resulting in a melting time reduction of 74.26% compared with the straight tube case. A numerical investigation has been performed by Alam et al. [25] to examine the heat transmission process in different LHTES models filled with PCM and various arrangements under simultaneous charging/discharging conditions. The cellular solids have

shown beneficial properties for heat transfer applications [26]. In Considering latent heat energy storage and MFs, Liu et al. [27] examined the combined effect of MF structures with porosity gradients and multiple PCMs to enhance melting performance. It was found that using multiple PCMs reduced the melting time by 9.18%, while a one-dimensional positive porosity gradient further decreased it by 6.18%. The optimal two-dimensional (2D) porosity gradient configuration achieved a 17.96% reduction in melting time and a 20.16% improvement in storage efficiency compared with a uniform MF with single PCM. Joshi and Rathod [28] innovated a novel configuration of LTES with the combination of pure PCM and metal foam PCM (MFPCM) system to optimize the utilization of MF in the MFPCM system. The results revealed that the novel configuration improved the overall melting rate. Seeking to enhance the thermal performance of the LTES, Joshi and Rathod [29] numerically optimized the allocation of MFPCM in the LTES, considering the volume of MFPCM and its distribution as an objective. The main finding is that compared with LTES with an entire volume of MF, the new configuration enhanced the melting rate by 11.11%. Mozaffari et al. [30] evaluated the effect of an engineered anisotropic metal foam layer (AMFL) on LHTES performance. The findings highlight that the AMFL improved paraffin melting by reducing the melting duration by up to 5.28%, and by 8.2% in the optimal AMFL orientation compared with a system with uniform MF. Buonomo et al. [31] numerically analyzed LTES with PCM and AMFL to explore the effect of nanoadditives on a pure PCM. Their results indicated that utilization of MF in addition to nanoadditives had a significant positive impact on heat transmission and melting and solidification times, while the complementary study of Ghalambaz et al. [32] demonstrated that combining copper foam with nano-enhanced PCM reduced the melting time by up to 50% with a 10% eccentricity in the porous layer, and by 12% due to the addition of nanoadditives, with copper nanoparticles performing slightly better than graphene oxide.

Moreover, Falcone et al. [33] performed an experimental study on LTES with pure paraffin (RT35) and CuMF-loaded paraffin. The experiment data indicated a positive impact of the CuMF-loaded PCM on heat transfer through the LTES and cycle time reduction. The augmentation of the thermal transport in LTES with fins and MF has been experimentally and numerically studied in [34]. The listed results exposed that MF outperforms fins as an LTES performance enhancer. Using a vacuum chamber and pressurized conditions, Esmaeili Shayan et al. [35] experimentally studied LTES using PCM and graphite foam with mixtures of different composites, such as salts and chloride salts. The results show a significant enhancement in the thermal conductivity of 45 times for the mixed compositions compared with pure PCM. Furthermore, Shu et al. [36] conducted a comprehensive investigation to study the influence of composite PCM latent heat storage systems during melting and solidification temperatures. Their findings revealed that increasing the heating temperature from 65°C to 85°C resulted in a 56% reduction in the total solid-to-liquid transition duration. Similarly, the solidification process was expedited by lowering the cooling temperature, where a decrease from 30°C to 10°C reduced the total liquid-to-solid transition duration by 40%. In addition to the aforementioned work on solidification, a recent study [37] numerically analyzed a circular LHTES unit under

partial charging and discharging conditions with three aluminum foam sheets spaced evenly at 120° , revealing that the configuration with the highest full charging power performs up to 6% worse during partial charging compared with other setups; moreover, a Y-shaped design charged in the upright orientation and discharged in an upside-down Y-shaped orientation achieved optimal overall performance. Yang et al. [38] explored the optimal radial and tangential placement of HTF tubes inside the flat-oriented shell-and-tube LHTES units during simultaneous charging and discharging processes. Their study demonstrated that the thermal performance was strongly affected by the positioning of HTF tubes, with energy delivery increasing by approximately 103% under the optimal configuration. A numerical research work [39] analyzed a double-pipe PCM heat exchanger and showed that the bottom position of the inner pipe minimized melting time, while the center position was optimal for solidification and cyclic processes due to conduction-dominated heat transfer. It was recommended to focus future studies on solidification enhancement. Additionally, Liang et al. [40] examined the thermal behavior of an LHTES device utilizing embedded flat micro-heat pipelines alongside an MF composite framework, offering valuable insights into its thermal properties. The equilibrium state and ultimate temperature of the PCM were not substantially influenced by the porosity of MF or the initial state of PCM, which was interesting. On the other hand, these variables did influence the duration necessary to achieve a steady-state condition. In addition, the results were not significantly affected by MF's pore density (pores per inch [PPI]). The findings consistently show that factors such as material composition, porosity, HTF arrangement, and temperature conditions play critical roles in enhancing melting rates, heat transfer, and overall system efficiency. These results underscore the potential for further optimization of LHTES configurations, particularly through the careful integration of PCM, MF, and novel geometrical designs.

Although numerous research works have explored the integration of MF and PCM in LHTES systems to enhance thermal performance, most have focused on uniform or anisotropic metal foam (AMF) configurations without adequately investigating the effects of varied geometries or strategic placements within the system. Furthermore, limited attention has been given to the effect of funnel-shaped AMF on the thermal fusion performance and heat distribution within LHTES systems. The current work addresses this gap by evaluating the thermal efficiency and melting behavior of partially AMF configurations, systematically varying their placement, coverage, and orientation to optimize heat absorption and distribution. By analyzing the present model, this study aims to reveal how directional heat condition and enhanced thermal dispersion affect the overall efficiency of LHTES systems. The necessity of this study lies in providing a deeper understanding of how specific AMF geometries can be utilized to improve heat transfer and phase change dynamics, ultimately leading to more efficient and stable energy storage solutions.

2 | Physical Problem

To enhance the melting efficiency of PCM in LHTES systems, this study investigates the optimal placement of anisotropic and uniform MF within the units, focusing on various funnel-shaped

configurations. The MFs can be manufactured with engineered properties as discussed in [41] where these structures impact the pressure drop and heat transfer [42, 43]. The setup is meticulously designed to capture and store excess thermal energy, thereby improving overall energy efficiency and management. As illustrated in Figure 1, the system features an intricate array of water channels that effectively distribute heat. These channels serve as conduits for the HTF, specifically water, which circulates and transfers heat to the PCM and is comprised of paraffin wax within a metallic foam of copper matrix. In this model, the HTF itself was not simulated; instead, its effect was represented by assuming a constant wall temperature. This approximation becomes more accurate as the flow rate in the channels increases. When the PCM is exposed to a temperature (T_h) above its fusion point (T_{fu}), it undergoes a phase transition from solid to liquid, absorbing and storing thermal energy in the process. The unit itself is housed within a sealed compartment measuring $15\text{ cm} \times 15\text{ cm}$, with thermal energy introduced from the left boundary, while the others are kept thermally insulated to minimize heat loss. Detailed internal configurations of the unit are shown in Figure 2, highlighting the combination of AMFL and a uniform layer. To guarantee a perpendicular alignment relative to the heat source, the thermal conductivity and permeability of the AMFL are influenced by directional characteristics, which are modulated through an anisotropy angle ($\omega = 0^\circ$) and an anisotropy parameter ($Kn = 0.3$). Special attention is given to the funnel-shaped structure, carefully designed to ameliorate heat absorption from the heated wall and promote even heat distribution throughout the PCM domain. This strategic dispersion mitigates direct heat exposure, promoting a more uniform melting of the PCM. The arrangement and dimensions of the AMFL are tailored, significantly affecting the thermal performance of the framework.

The AMFL coverage is designed to start at 36% in configurations a1, b1, c1, and d1, with an 8% increase in each subsequent configuration, culminating at 60% coverage in a4, b4, c4, and d4. The designs are grouped into four categories, each progressively increasing the proportion of AMFL. Group a (a1–a4) starts with 36% AMFL coverage in a1 and increases through 44%, 52%, to 60% in a4, exploring the effect of AMFL coverage on thermal efficiency. Group b (b1–b4) reverses the configuration of Group a, starting at 36% and reaching 60%, allowing for a comparison of how AMFL orientation influences heat transfer. Group c (c1–c4) follows the same percentage pattern as Group a, with AMFL coverage starting at 36%, progressing through 44%, 52%, and reaching 60%, but with a larger AMFL area, enhancing heat absorption and PCM melting efficiency. Group d (d1–d4) mirrors Group c's expansion but reverses the shape, focusing on the impact of extensive AMFL coverage on thermal management and stability.

3 | Governing Equations

The core equations governing mass, momentum, and energy within the LHTES are represented by partial differential equations. The investigation considers three distinct regions: the copper conduit layer, the AMFL-PCM composite, and the regular MF-PCM mixture. The model treats the liquefied PCM as a Newtonian fluid with noncompressible volume under 2D laminar flow conditions and employs the Boussinesq approximation to manage density fluctuations and temperature variations,

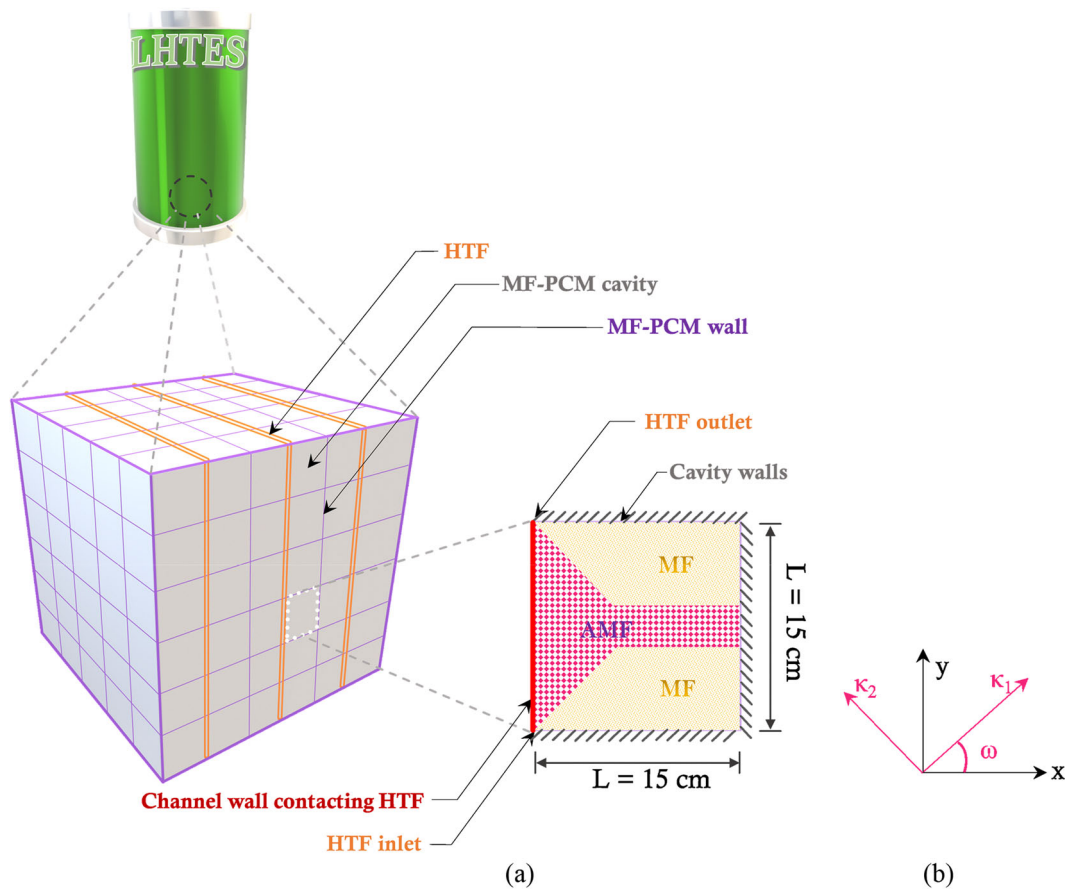


FIGURE 1 | Visualization of the multichannel LHTES setup, depicting the entry point for the HTF alongside a two-dimensional sectional representation of the thermal storage chamber. (a) Schematic of the storage chamber and (b) positional alignment concerning anisotropic angle variations (ω). HTF, heat transfer fluid; LHTES, latent heat thermal energy storage; MF, metal foam; PCM, phase change material. [Color figure can be viewed at [wileyonlinelibrary.com](https://onlinelibrary.wiley.com/doi/10.1002/ht.23387)]

with no slip velocity near the walls. Some local anisotropic effects in the Representative Elementary Volume (REV) can be expected due to the anisotropic nature of the foam structure. However, the natural convection flow forms on a scale much larger than REV, and the liquid PCM flows between cells. Thus, such a local anisotropic body forced at the REV level would not impact the natural convection flow in a notable way on the domain scale.

Whether in uniform or anisotropic configurations, fluid behavior is examined through continuity and momentum equations, addressing natural convection phenomena. Specific adjustments in permeability and porosity tailor the behavior of the PCM and MF, while coupling source terms ensure integrated energy transfer across different phases. The Darcy–Brinkman–Forchheimer method establishes a basis for modeling fluid flow with porous structures, facilitating an in-depth study of the system's hydrodynamics. At the same time, the local thermal nonequilibrium model is incorporated into the energy balance equations to control heat exchange independently in each phase. To capture phase transitions, the enthalpy-porosity approach is utilized, likening the partially melted state in the mushy region to fluid transport in porous channels. This method embeds custom terms into the momentum equations to represent the restrictive influence of solidified PCM, dictated by the melt fraction (ϕ). Additionally, the x-directional momentum equation has been enhanced to include

2D flow porosity (ε) and variable density (ρ_{wax}), integrating a source term to adjust fluid momentum in response to the liquid fraction $\phi(T)$. The configuration allows for precise simulation of phase transitions and fluid dynamics in the system [44–46].

$$\frac{1}{\varepsilon} \rho_{\text{wax}} \left(\frac{\partial u}{\partial t} \right) + \frac{1}{\varepsilon^2} \rho_{\text{wax}} \left(u \frac{\partial u}{\partial x} + v \frac{\partial u}{\partial y} \right) = - \left(\frac{\partial p}{\partial x} \right) + \frac{1}{\varepsilon} \mu_{\text{wax}} \left(\frac{\partial^2 u}{\partial x^2} + \frac{\partial^2 u}{\partial y^2} \right) + \left(- \frac{\mu_{\text{wax}}}{\kappa} - \frac{\rho_{\text{wax}} C_F |U|}{\sqrt{\kappa}} + \frac{A_{\text{mush}} (1 - \phi(T))^2}{\gamma_{\text{mush}} + \phi^3(T)} \right) u. \quad (1)$$

The momentum equation along the y-axis includes factors like heat transfer via convection, emphasizing the influence of buoyancy-driven flow within the liquefied PCM. The terms corresponding to the copper MF, paraffin-wax are denoted as “copper,” “wax,” and “eff,” respectively. This y-axis momentum equation is expressed as

$$\frac{1}{\varepsilon} \rho_{\text{wax}} \left(\frac{\partial v}{\partial t} \right) + \frac{1}{\varepsilon^2} \rho_{\text{wax}} \left(u \frac{\partial v}{\partial x} + v \frac{\partial v}{\partial y} \right) = - \left(\frac{\partial p}{\partial y} \right) + \frac{1}{\varepsilon} \mu_{\text{wax}} \left(\frac{\partial^2 v}{\partial x^2} + \frac{\partial^2 v}{\partial y^2} \right) + g \rho_{\text{wax}} \beta_{\text{wax}} (T - T_0) + \left(- \frac{\mu_{\text{wax}}}{\kappa} - \frac{\rho_{\text{wax}} C_F |U|}{\sqrt{\kappa}} + \frac{A_{\text{mush}} (1 - \phi(T))^2}{\gamma_{\text{mush}} + \phi^3(T)} \right) v. \quad (2)$$

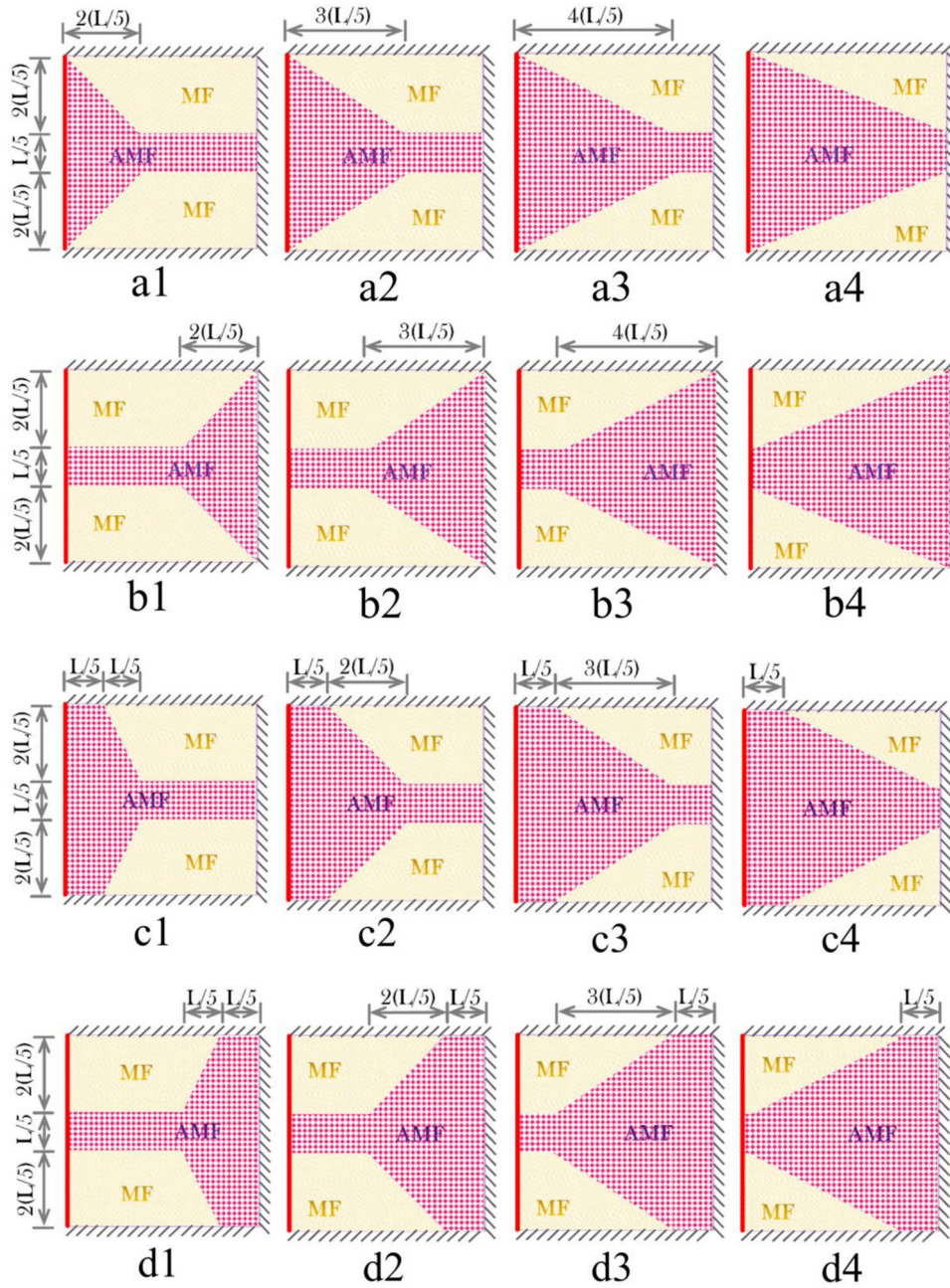


FIGURE 2 | A funnel-shaped layer of anisotropic metal foam (AMF), showing AMFL growth in 8% increments: a1, b1, c1, d1 at 36%; a2, b2, c2, d2 at 44%; a3, b3, c3, d3 at 52%; a4, b4, c4, d4 at 60% coverage of the overall MF zone. Uniform MF fills the other regions. AMFL, anisotropic metal foam layer; MF, metal foam. [Color figure can be viewed at [wileyonlinelibrary.com](https://onlinelibrary.wiley.com/doi/10.1002/hj.23387)]

Energy conservation within the PCM region is examined, highlighting the convective heat transfer interaction between the PCM and surrounding copper, as well as the internal heat diffusion within the PCM layer. Since the PCM is embedded in MF, the effective thermal conductivities for the MF ($k_{\text{eff,copper}}$) and PCM ($k_{\text{eff,wax}}$) were used. The energy conservation in the PCM phase is represented by [47]

$$\begin{aligned} \varepsilon(\rho C_p)_{\text{wax}} \frac{\partial T_{\text{wax}}}{\partial t} + (\rho C_p)_{\text{wax}} \left(u \frac{\partial T_{\text{wax}}}{\partial x} + v \frac{\partial T_{\text{wax}}}{\partial y} \right) \\ = k_{\text{eff,wax}} \left(\frac{\partial^2 T}{\partial x^2} + \frac{\partial^2 T}{\partial y^2} \right) + h_v (T_{\text{copper}} - T_{\text{wax}}) - \varepsilon \rho_{\text{wax}} L_{\text{wax}} \frac{\partial \phi(T)}{\partial t}. \end{aligned} \quad (3)$$

In the MF region, the equation underscores thermal energy balance. The MF structures occupy $(1 - \varepsilon)$ amount of space with a heat capacity of $(1 - \varepsilon)(\rho C_p)_{\text{copper}}$:

$$\begin{aligned} (1 - \varepsilon)(\rho C_p)_{\text{copper}} \frac{\partial T_{\text{copper}}}{\partial t} = k_{\text{eff,copper}} \left(\frac{\partial^2 T_{\text{copper}}}{\partial x^2} + \frac{\partial^2 T_{\text{copper}}}{\partial y^2} \right) \\ + h_v (T_{\text{wax}} - T_{\text{copper}}). \end{aligned} \quad (4)$$

The thermophysical attributes are derived using a linearly weighted averaging method. The mathematical framework incorporates key variables, such as the thermal expansion

TABLE 1 | Characteristics of materials: Metal foam and paraffin wax.

| Materials | ρ (kg/m ³) | μ (Pa·s) | T_{fu} (K) | C_p (J/(kg·K)) | k (W/(m·K)) | Fusion enthalpy (J/kg) |
|--|--------------------------------|--------------|--------------|---------------------|------------------|---------------------------|
| Paraffin (solid/liquid) [51–53, 55] | 916/790 | 0.0036 | 324.65 | 2700/2900 | 0.21/0.12 | 176,000 |
| Copper foam [56] | 8900 | — | — | 386 | 380 | — |

rate (β), porous permeability (κ), fusion enthalpy (L), and the Forchheimer drag coefficient (C_F). The equations differentiate between the liquid phase (l) and solid phase (s) of the paraffin wax:

$$(\rho C_p)_{wax} = \phi(\rho C_p)_s + (1 - \phi)(\rho C_p)_l, \quad (5)$$

$$\rho_{wax} = \phi\rho_s + (1 - \phi)\rho_l. \quad (6)$$

The mushy region is modeled by a porous medium, where the shift from liquid to solid significantly decreases permeability and porosity, resulting in minimal fluid motion and underscoring the suppressive impact of body forces in this region. In the melting process, the parameter A_{mush} in the Carman–Kozeny equation plays an important role in controlling the velocities of the PCM, reflecting the structure of the melting front. It sets values from 6E6 Pa·s/m² for unobstructed flow to 1×10^{10} Pa·s/m² within the MF area, managing flow in solidified sections by reducing velocity as it approaches the solid phase, making a transition zone. To maintain numerical stability and avoid singularities, a minor parameter, γ_{mush} , assigned a value of 0.001, is incorporated to support the model's computations. The PCM liquid fraction ϕ , dependent on temperature, is outlined as follows [5]:

$$\phi(T) = \begin{cases} 0, & T < T_{fu} - \frac{\Delta T_{fu}}{2} \text{ (solid wax),} \\ \frac{(T - T_{fu})}{\Delta T_{fu}} + \frac{1}{2}, & T_{fu} - \frac{\Delta T_{fu}}{2} \leq T \leq T_{fu} + \frac{\Delta T_{fu}}{2} \\ & \text{(mushy area),} \\ 1, & T > T_{fu} + \frac{\Delta T_{fu}}{2} \text{ (liquid wax).} \end{cases} \quad (7)$$

In the mushy zone, the paraffin wax undergoes a phase change from solid to liquid over a specified temperature interval denoted by ΔT_{fu} , where T_{fu} signifies the melting temperature. The function $\phi(T)$ serves as a linear approximation to the transition between the two states. In this intermediate phase, the PCM simultaneously contains both solid and liquid components. The viscosity is determined by the equation $\mu = (1 - \phi) \times a + \mu_{wax,l}\phi$, where a is assigned a substantial magnitude of 10^4 Pa·s, representing the resistance of the solid phase for any fluid motion. When $\phi = 1$, then $\mu_{wax,l}$, and as ϕ approaches zero in the solidified regions, the viscosity increases gradually, thereby amplifying resistance to fluid movement [5]. An equation cited in various sources [44, 47] was applied to determine the PCM's thermal conductivity, where $k_{eff,wax} = k_{wax}(2 + \varepsilon)/3$, underscoring the porosity in the MF.

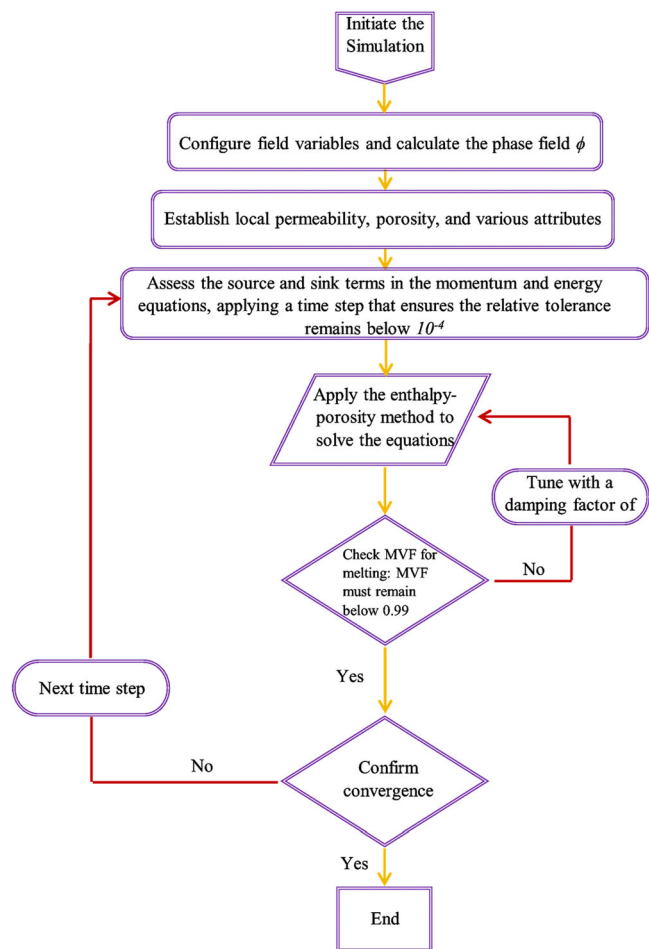


FIGURE 3 | Schematic of the simulation procedure employed to solve the mathematical equations for phase change material melting. MVF, melted volume fraction. [Color figure can be viewed at [wileyonlinelibrary.com](https://onlinelibrary.wiley.com/terms-and-conditions)]

The ligaments in the MF layer are strategically aligned and fortified along a defined axis to optimize heat conduction and alter permeability [48, 49]. These characteristics are regulated by the anisotropy parameter (Kn) and the anisotropy angle (ω). This approach acknowledges changes in thermal conductivity and permeability due to directional changes in the design of the funnel-shaped AMFL. The equations that detail this anisotropic behavior utilize trigonometric functions of ω to translate properties between the principal and actual directions. A second-order tensor is employed to link the intrinsic properties, k_1 and k_2 , with the anisotropy angle, as elaborated in the subsequent equations [49, 50]:

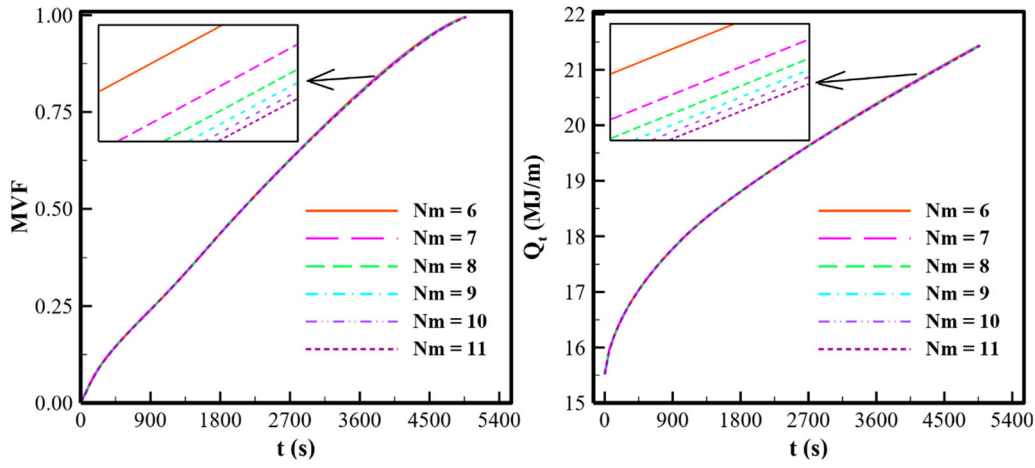


FIGURE 4 | Mesh analysis: Evaluating MVF and Q_t across Nm values 6, 7, 8, 9, 10, and 11. MVF, melted volume fraction. [Color figure can be viewed at [wileyonlinelibrary.com](https://onlinelibrary.wiley.com)]

TABLE 2 | Computational durations across varying Nm cases.

| Nm | Time needed |
|------|------------------------|
| 6 | 3 h, 3 min, and 50 s |
| 7 | 5 h, 40 min, and 12 s |
| 8 | 9 h, 1 min, and 46 s |
| 9 | 12 h, 40 min, and 10 s |
| 10 | 17 h, 14 min, and 47 s |
| 11 | 22 h, 32 min, and 29 s |

$$\kappa = \left[\frac{\kappa_2 (\sin \omega)^2 + \kappa_1 (\cos \omega)^2 (\kappa_1 - \kappa_2) (\cos \omega) (\sin \omega)}{(\kappa_1 - \kappa_2) (\cos \omega) (\sin \omega) \kappa_2 (\cos \omega)^2 + \kappa_1 (\sin \omega)^2} \right], \quad (8a)$$

$$k_{\text{eff, copper}} = \left[\frac{k_2 (\sin \omega)^2 + k_1 (\cos \omega)^2 (k_1 - k_2) (\sin \omega) (\cos \omega)}{(k_1 - k_2) (\sin \omega) (\cos \omega) k_2 (\cos \omega)^2 + k_1 (\sin \omega)^2} \right]. \quad (8b)$$

The copper MF's average thermal conductivity (k_m) and permeability (κ_m) are computed based on the following relations: $k_1 = (1 + Kn) \times k_m$ and $k_2 = (1 - Kn) \times k_m$. Corresponding formulas for permeability are $\kappa_1 = (1 - Kn) \times \kappa_m$ and $\kappa_2 = (1 + Kn) \times \kappa_m$. These calculations derive from methodologies detailed in references [30, 51–53]. The anisotropy factor, represented by Kn , where a value of $Kn = 0$ indicates an isotropic MF, plays a main role in maintaining the structural integrity of the MF. It is essential to manage the anisotropic factor to ensure practical functionality. Furthermore, the thermophysical properties in the mushy area are determined using a linear weight average method. The copper MF's mean permeability (κ_a) and effective thermal conductivity, $k_a = k_{\text{copper}}(1 - \varepsilon)/3$, have also been calculated, including findings from prior research [44, 47, 54], to maintain the structure and performance of the MF:

$$\kappa_a = \frac{1}{(\kappa_{\text{tor}} - 1) \kappa_{\text{tor}}} \left(\frac{\varepsilon d_{\text{fp}} \sqrt{\frac{\kappa_{\text{tor}}}{3\varepsilon}}}{6} \right)^2. \quad (9)$$

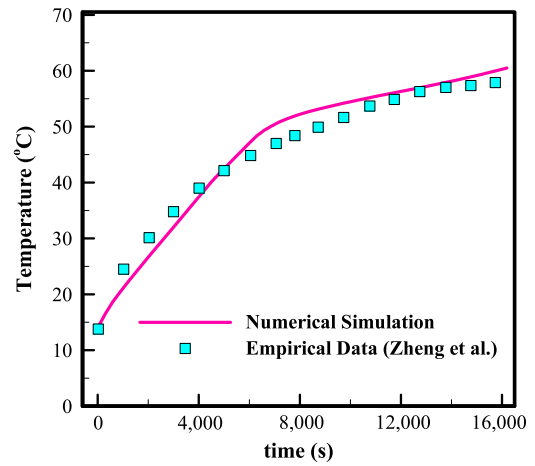


FIGURE 5 | Validation of study results through comparison with empirical data from [56]. [Color figure can be viewed at [wileyonlinelibrary.com](https://onlinelibrary.wiley.com)]

It is vital to incorporate equations that involve κ_{tor} and d_{fs} to assess the thermal properties of the MF material. These calculations are instrumental in determining the thermal conductivity of copper (k_{copper}), the PPI parameter ($d_{\text{fp}} = 0.0254/\text{PPI}$), with the MF's overall thermal conductivity, as noted in reference [54]:

$$\frac{1}{\kappa_{\text{tor}}} = \frac{(9 - 8\varepsilon)^{\frac{1}{2}}}{2\varepsilon} \cos \left\{ \frac{4\pi}{3} + \frac{1}{3} \cos^{-1} \left(\frac{8\varepsilon^2 - 36\varepsilon + 27}{(9 - 8\varepsilon)^{\frac{3}{2}}} \right) \right\} \quad (10)$$

$$d_{\text{fp}} + \frac{3}{4\varepsilon},$$

$$\frac{d_{\text{fs}}}{d_{\text{fp}}} = \left(\frac{59}{50} \right) \left(\frac{1}{1 - \exp(25(\varepsilon - 1))} \right) \left(\frac{1 - \varepsilon}{3\pi} \right)^{\frac{1}{2}}. \quad (11)$$

Additionally, the analysis included the calculation of the Forchheimer coefficient (C_F) as detailed here [54]:

$$C_F = \left(\frac{d_{\text{fs}}}{d_{\text{fp}}} \right)^{-1.63} (1 - \varepsilon)^{-0.132} \times 0.00212. \quad (12)$$

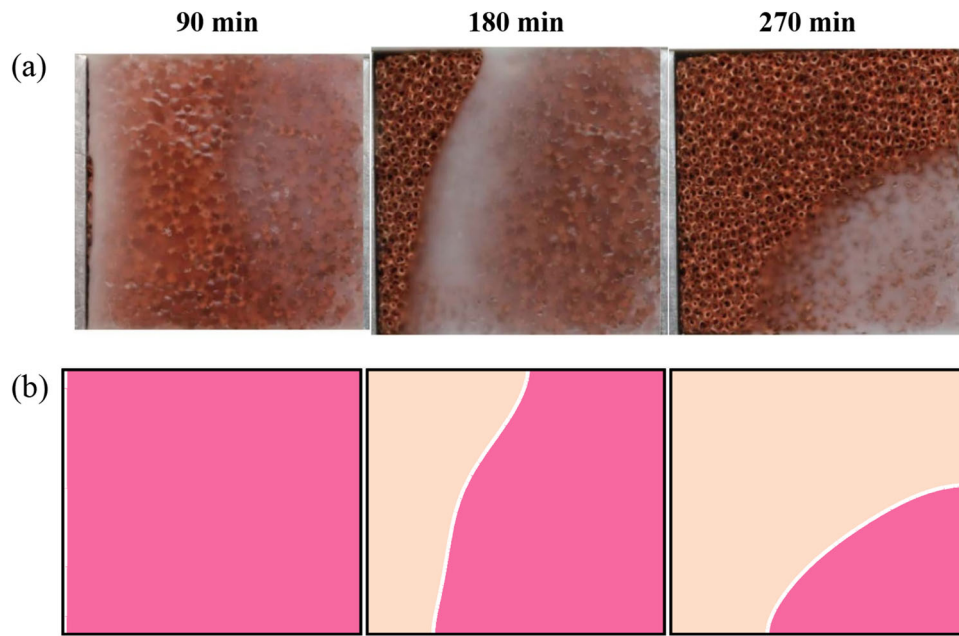


FIGURE 6 | Advancement of melting in the PCM-MF hybrid paraffin within a square enclosure: (a) experimental data from [56] and (b) results from our current study. MF, metal foam; PCM, phase change material. [Color figure can be viewed at [wileyonlinelibrary.com](https://onlinelibrary.wiley.com/doi/10.1002/hj.23387)]

The melting process in the PCM is tracked by the melted volume fraction (MVF), which serves as a key indicator for evaluating thermal energy storage as the PCM undergoes its phase transitions. The MVF, a nondimensional measure, quantifies the extent of the PCM's liquefaction relative to its total volume. To compute this fraction, an integral ratio is determined over the designated volumetric region. Zero MVF signifies that the PCM remains entirely solid, while a value of one represents complete melting into the liquid phase.

$$\text{MVF} = \frac{\oint_V (\varepsilon \phi) dV}{\oint_V (\varepsilon) dV}. \quad (13)$$

The rate of energy storage in the system is derived by dividing the total stored energy (Q_{store}) by the duration over which this energy is accumulated.

$$\text{Power} = \frac{Q_{\text{store}}}{\text{time}} = \frac{Q_{\text{latent}} + Q_{\text{sensible}}}{\text{time}}, \quad (14a)$$

$$Q_{\text{latent}} = \varepsilon \oint_V (\rho_{\text{wax}} \phi L_{\text{wax}}) dV. \quad (14b)$$

Equation (14b) focuses on calculating the total latent heat stored as the PCM transitions between solid and liquid states. The overall energy retention, Q_{store} , encompasses the combined values of sensible (Q_{sensible}) and latent (Q_{latent}) heat energies. Thus, the stored energy includes the contributions from both solid and liquid phases of the PCM, the HTF, and the system's wall.

Table 1 outlines the paraffin's thermophysical characteristics, which serves as the PCM, and copper foam, acting as the MF, both integral to the performance of LHTES units. These materials are essential in optimizing the efficiency and reliability of

TABLE 3 | Total melting duration for each setting at $Kn = 0.3$ and $\omega = 0^\circ$.

| Cases | AMFL coverage percentage (%) | Melting time (s) | | |
|-------|------------------------------|------------------|---------|---------|
| | | 80% | 90% | 99.5% |
| a1 | 36 | 3515.45 | 4105.00 | 4867.14 |
| a2 | 44 | 3460.14 | 4046.22 | 4807.12 |
| a3 | 52 | 3453.37 | 4033.05 | 4787.85 |
| a4 | 60 | 3455.79 | 4035.58 | 4788.74 |
| b1 | 36 | 3717.74 | 4329.31 | 5114.92 |
| b2 | 44 | 3701.87 | 4303.77 | 5083.23 |
| b3 | 52 | 3650.62 | 4242.92 | 5020.50 |
| b4 | 60 | 3607.18 | 4196.56 | 4972.07 |
| c1 | 36 | 3505.53 | 4096.22 | 4862.07 |
| c2 | 44 | 3440.27 | 4026.30 | 4791.84 |
| c3 | 52 | 3426.04 | 4003.41 | 4761.20 |
| c4 | 60 | 3430.89 | 4010.02 | 4766.47 |
| d1 | 36 | 3714.67 | 4316.72 | 5101.34 |
| d2 | 44 | 3712.08 | 4314.75 | 5097.13 |
| d3 | 52 | 3657.11 | 4254.30 | 5034.29 |
| d4 | 60 | 3597.88 | 4189.60 | 4969.18 |

Abbreviation: AMFL, anisotropic metal foam layer.

energy systems by enhancing both the capacity for heat storage and the rate of thermal conduction. The paraffin wax effectively controls energy variations via its phase transition, whereas the MF plays a key role in improving heat distribution and consistency throughout the system, ensuring more efficient thermal exchange.

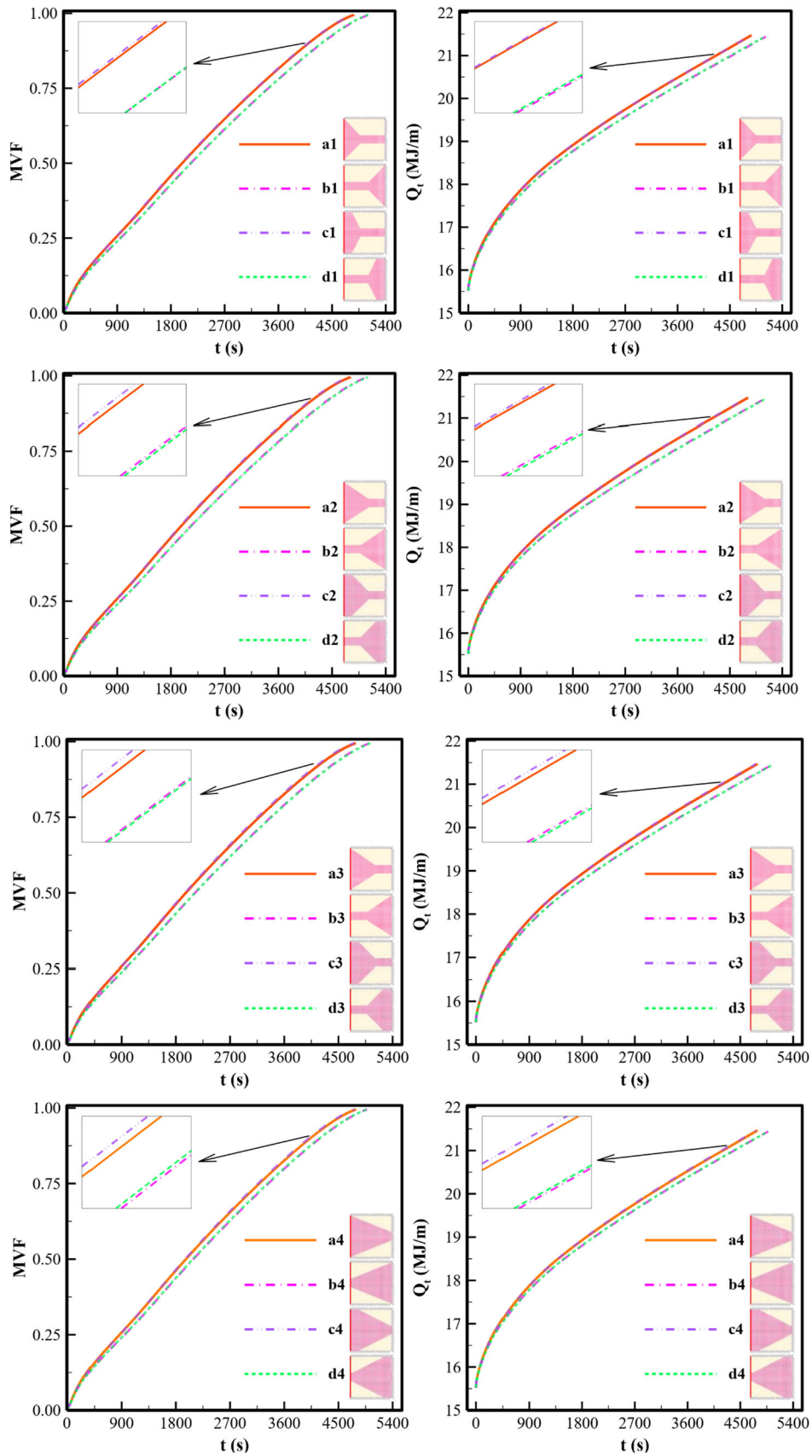


FIGURE 7 | MVF and Q_t across various configurations during melting at $Kn = 0.3$ and $\omega = 0^\circ$. MVF, melted volume fraction. [Color figure can be viewed at [wileyonlinelibrary.com](https://onlinelibrary.wiley.com/doi/10.1002/ht.23387)]

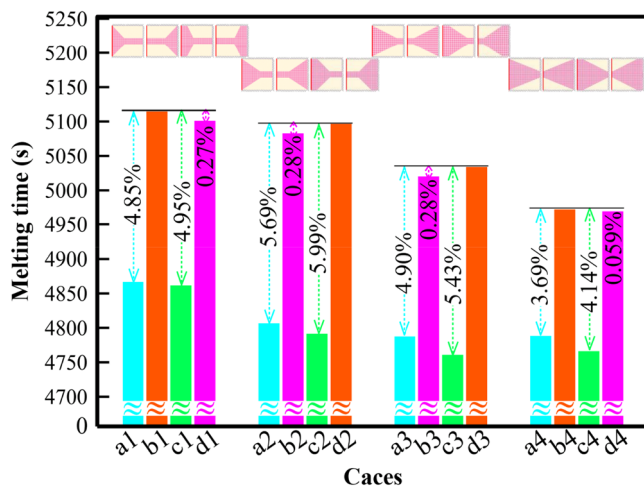


FIGURE 8 | Melting times for configurations at $Kn=0.3$ and $\omega=0^\circ$. Each column illustrates the percentage reduction in the solid-to-liquid transition time, compared with the least effective group, marked in red, while the most effective group is highlighted in green. [Color figure can be viewed at [wileyonlinelibrary.com](https://onlinelibrary.wiley.com)]

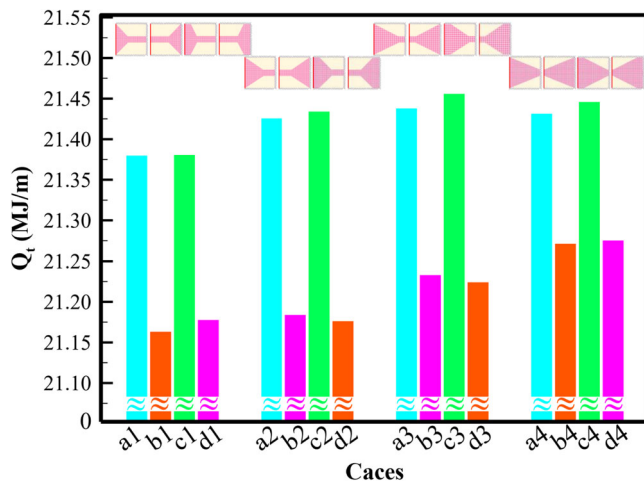


FIGURE 9 | Energy stored at $t=4750$ s for various scenarios at $Kn=0.3$ and $\omega=0^\circ$. The least efficient designs are marked in red, and the most efficient designs are marked in green across scales. [Color figure can be viewed at [wileyonlinelibrary.com](https://onlinelibrary.wiley.com)]

With the specified boundary and initial conditions, all walls were assumed to have no velocity. The temperature of the heated wall was set to $T_w = 339.8$ K, and the initial temperature was defined as a significantly lower value of 324.65 K. The finite element method (FEM) was adopted to ensure robust and accurate results across the computational grid, proving it to be the ideal technique for the study's aims, with a reference pressure set to zero at the upper-left corner of the domain. The simulations commenced with these starting conditions to assess energy storage and phase change dynamics. The thermal and continuity equations, along with the phase field variable, were solved iteratively. The simulation ended when the MVF exceeded 0.99, indicating almost complete melting. Figure 3 provides an outline of the computational algorithm used to track the evolution of the melting process. Generating a set of algebraic residual equations, FEM integrates the governing equations over discrete elements using Gauss quadrature. These

residuals were solved iteratively using the PARSIDO solver to deliver precise results. The time-step was automatically controlled using the backward differentiation formula of second order to maintain the solver accuracy within the relative error threshold of 10^{-4} .

4 | Mesh Sensitivity Analysis

The study probed the impact of mesh resolution on the accuracy of numerical simulations concerning phase change processes in the cavity, with a focus on the fusion behavior of the PCM under specific configurations, notably design b4 with $Kn=0.3$ and $\omega=0^\circ$. Utilizing a nonuniform mesh to segment the computational domain, the density of the mesh, denoted as Nm , was varied to assess its effect on simulation outcomes. It was observed that a mesh setting of $Nm=8$ was particularly effective, balancing simulation accuracy and computational time, which totaled approximately 9 h and 1 min during complete melting for design b4. Further details on how mesh configurations influence the simulation are available in Figure 4, which compares the time required for complete melting across different mesh densities ranging between $Nm=6$ and 11. Additionally, Table 2 demonstrates the computational demands associated with varying resolutions; the simulation time extends from 3 h and 3 min at the lowest density ($Nm=6$) to 22 h and 32 min at the highest ($Nm=11$). This increment in time with denser meshes reflects a more detailed capture of heat transfer processes, but increases computational load as well. The analysis demonstrates that higher mesh densities, while providing more detailed insights into heat transfer, require considerably more computational resources. Conversely, lower densities expedite simulations but at the cost of detail and accuracy. Ultimately, the selected mesh resolution of $Nm=8$ offers an optimal compromise, ensuring sufficient detail for accurate simulations without overly taxing computational resources. This strategic choice aids in optimizing both the design and operational efficiency of LHTES systems under various conditions.

5 | Simulation Validation

In the investigation by Zheng et al., referenced in [56], an in-depth study of the melting properties of a copper foam/paraffin composite PCM was carried out within a rectangular polyethylene casing. The research involved testing various heat application points, left, bottom, and top, to observe the solid-to-liquid dynamics. Notably, the left boundary was exposed to a constant heat flux of 1150 W, with a temperature rise of $10^\circ\text{C}/\text{min}$, and the others were kept thermally insulated. The empirical configuration utilized a $100 \times 10 \times 30$ mm electrical heater to examine the temperature distribution and the progression of the phase interface. The system was thermally maintained between 20°C and 80°C under steady laminar flow conditions, exhibiting significant thermal sensitivity. The melting properties of the paraffin wax were significantly impacted by the copper foam's porosity of 0.95 and its pore density of 5 per inch. This structure notably accelerated heat transfer within the PCM, thereby enhancing the effective

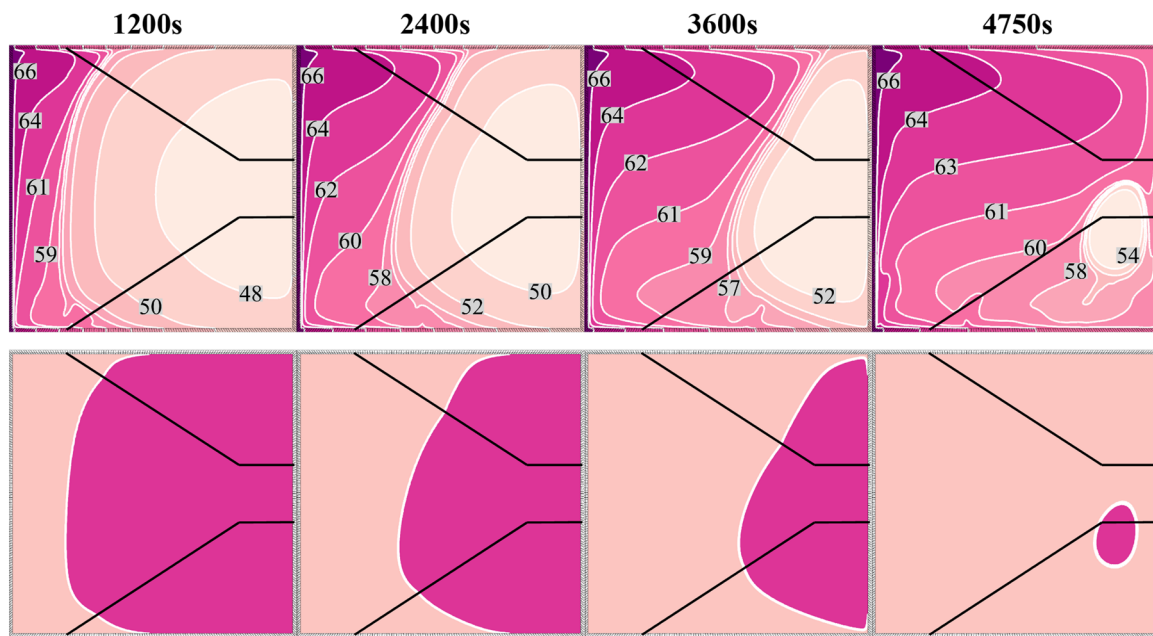


FIGURE 10 | Celsius isotherms and MVF contours for configuration c3. In the MVF contours, the lighter color zones denote the melted phase of PCM, while the darker color zone indicates the solid phase. MVF, melted volume fraction; PCM, phase change material. [Color figure can be viewed at [wileyonlinelibrary.com](https://onlinelibrary.wiley.com/doi/10.1002/hj.23387)]

thermal conductivity of the composite. Figures 5 and 6 in the study detail the thermal performance and phase change characteristics, respectively. Figure 4 presents a mean temperature profile in the vertical direction situated 2.5 cm from the heat source, juxtaposing empirical outcomes with numerical predictions across various intervals. The consistent agreement between these observations and the simulations underscores the precision of the modeling efforts. Figure 6, meanwhile, depicts the phase transition of the PCM from liquid to solid at different intervals, showing the fidelity of the simulation in mirroring the experimental results in terms of structural detail, edge clarity, and thermal gradients. This congruence reinforces the reliability of the numerical model as validated by the empirical data.

6 | Results and Discussion

The current study aims to optimize the melting time of PCM in LHTES systems by evaluating the placement of anisotropic and uniform MF within the units. The system features water channels for heat distribution, with the PCM (paraffin wax) melting in a copper MF matrix when exposed to heat from one side, while other boundaries are insulated. Various funnel-shaped configurations of MF, with different coverages (36%–60%), are analyzed for their impact on thermal efficiency.

Table 3 represents the total melting duration for the different configurations shown in Figure 2. The melting time in all the cases is in the same order of magnitude. It is noted that the configurations a and c have, on average, shorter total melting durations compared with the configurations b and d, respectively. As a first observation, this indicates that arranging the longer side of the funnel-shaped AMFL adjacent to the heated wall results in accelerated PCM melting. It is also seen that in

configurations a–d, the melting time gets reduced from cases 1 to 4, that is, when the percentage of the AMFL is raised. This is an indicator that replacing parts of the isotropic MF with an anisotropic porous one can indeed help in enhancing PCM melting inside the enclosure. As a last observation that can be extracted from this table, it is seen that the melting times in configurations a and c are almost equal, with very slight reduction in c compared with a. This means that extending the shape of the AMFL near the heated wall can slightly enhance melting, but less importantly than placing the large side near the hot wall. A similar note can be found when comparing configurations b and d.

Figure 7 shows the fluctuations in the MVF and the stored thermal energy (Q_t) as a function of time across the various setups. In all cases, both the MVF and Q_t increase from zero over time as the initially solid PCM melts near the heated wall until it becomes fully liquid when MVF reaches 1. Q_t initially rises abruptly at the onset of melting, then as the quantity of solid PCM is reduced, Q_t keeps rising but at a lower slope. As for the case-to-case comparison, it is seen that in each configuration, the MVF and Q_t are slightly higher in cases a and c compared with cases b and d. This is due to the fact that the larger part of the AMFL is at the hot wall. As the PCM starts melting in that region, the increase of the permeability in the direction of the flow enhances the convective effects, which result in increased melting and consequent stored thermal energy.

The melting times for each configuration are plotted in Figure 8, with an indication of the case with minimum time for comparison. It is clear that in all the configurations, the least effective melting occurs in the case where the large size of the funnel-shaped AMFL is placed at the cold wall. In group 1, where the AMFL occupies 36% of the total meatal foam area,

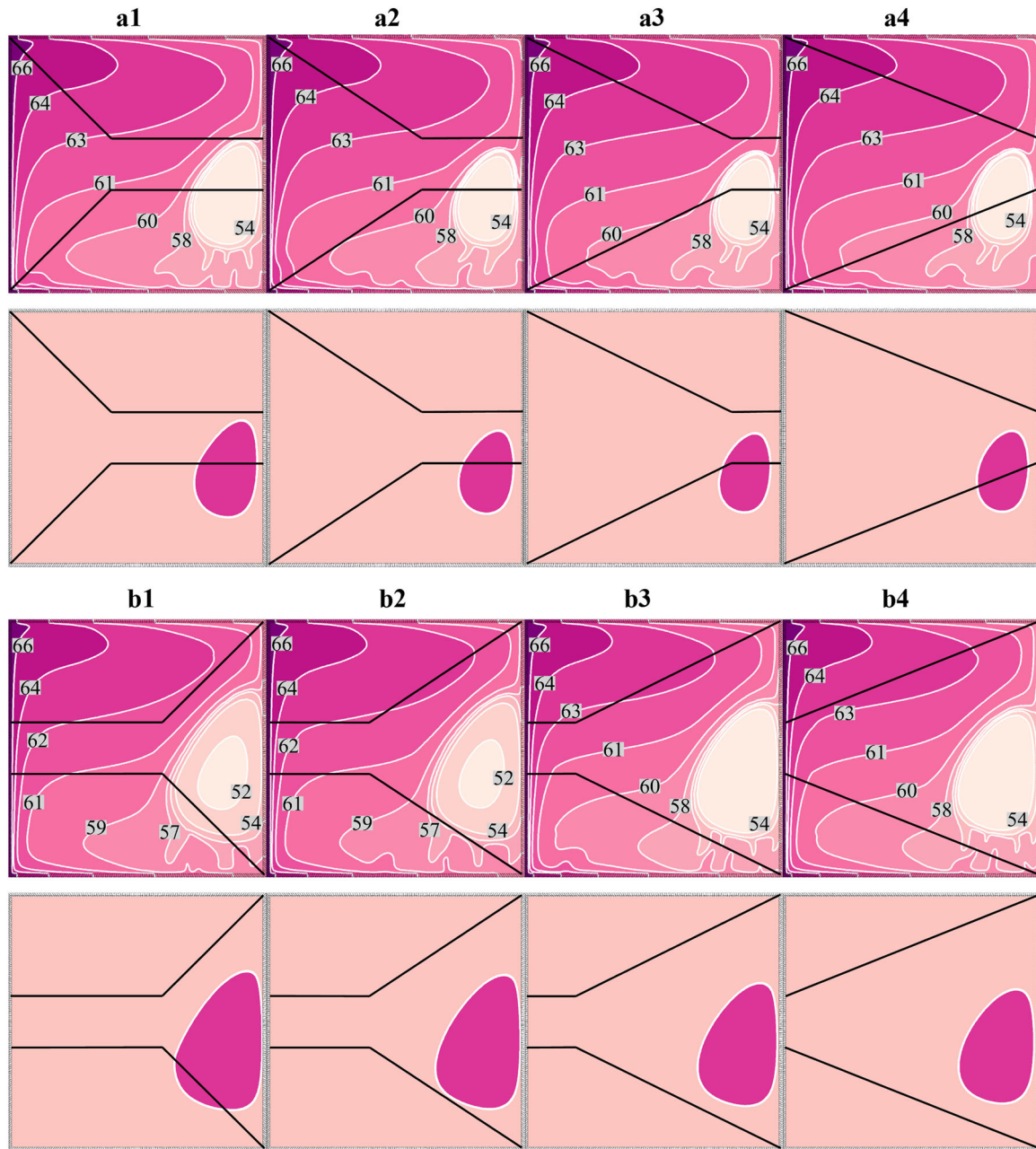


FIGURE 11 | At $t = 4750$ s, displaying isotherms in Celsius and MVF contours for all configurations at $Kn = 0.3$ and $\omega = 0^\circ$. In the MVF contours, the melted phase of PCM is shown in the lighter color zone, whereas the solid phase is shown in the darker color zone. MVF, melted volume fraction; PCM, phase change material. [Color figure can be viewed at [wileyonlinelibrary.com](https://onlinelibrary.wiley.com/doi/10.1002/htj.23387)]

moving the bulky portion of the AMFL from the right to the left increases the melting rate by around 4.9%. In group 2, where 44% of the MF is covered by AMFL, making the same change in the funnel shape leads to a 5.8% decrease in total melting duration. This variation in melting time changes to 5.1% and 3.9% in groups 3 and 4, where the AMFL covers 52% and 60% of the total MF area, respectively. It is worth noting that expanding the AMFL shape offers a negligible impact on the melting speed, as less than 0.3% change is found between cases b and d. In addition, increasing the size of the AMFL while keeping the same geometrical configuration leads to faster melting. For instance, increasing the covering percentage of the AMFL from 36% to 60% reduces the melting duration by 2.1% when the large size of the funnel shape is

placed at the hot wall (configuration c) and by 3.1% when it is at the cold wall (case b).

The energy stored Q_t after 4750 s for each configuration is shown in Figure 9. The change in Q_t follows one of the MVFs in the sense that the cases with the shortest melting times provide the highest values of Q_t due to the effective melting and the resulting stored heat. In addition, for a given geometrical configuration, Q_t increases for higher AMFL percentage (groups 1–4). It should be noted that, like in the case of the MVF, the impact of the geometrical arrangement of the funnel shape on Q_t is more important than the percentage of the AMFL in the enclosure. For comparison, Q_t in configuration c1 is higher than in configuration d3, even though the percentage of the AMFL in

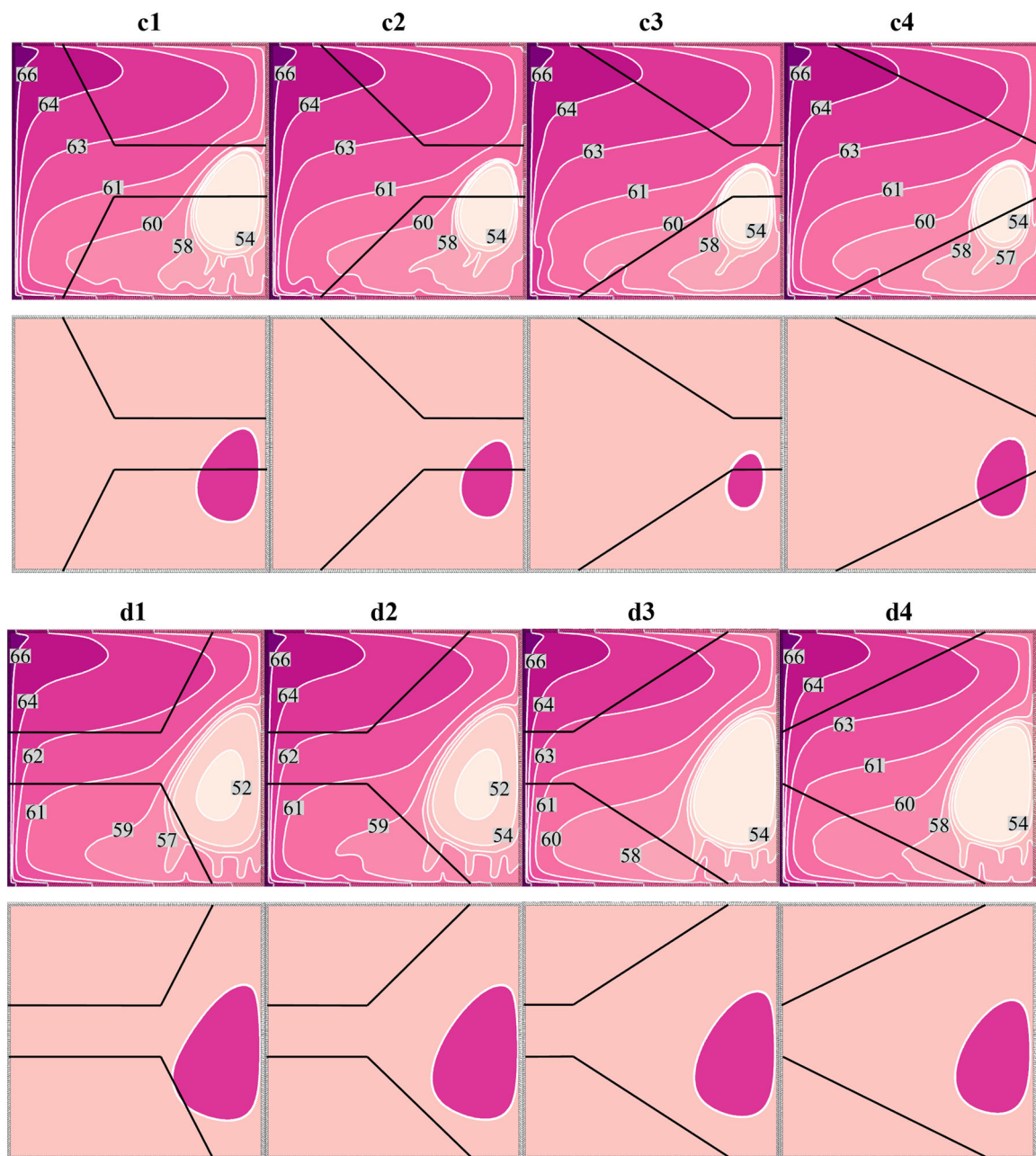


FIGURE 11 | (Continued)

the latter is 52%, while it is 36% in the former. This is an indicator that placing an AMFL in the cavity alone is not sufficient to optimize the PCM melting performance. The optimal configuration consists of orienting the anisotropic layer in the direction where the high permeability is along the convective flow. Once this is achieved, further increasing the size of the AMFL can help achieve even higher performance.

To better understand the impact of the AMFL on the local behavior of the PCM, an analysis of the temperature and melting distribution inside the cavity is required. In this regard, Figure 10 illustrates the contours of temperature and MVF for the efficient configuration (c3). Initially, a small amount of PCM melts along the left wall, creating a thin vertical layer of liquid PCM in that region. The isotherms there are vertical, indicating that heat transfer occurs by conduction. As time goes

on, more PCM melts, and thermal convection starts taking place as the hot PCM moves upward and is replaced by a descending colder PCM. After a longer time, the convection dominates the heat transfer, and the isotherms become horizontal in the center of the cavity. The initiation of heat transfer and convective flow in the region near the hot wall illustrates the reason why the AMFL shape affects the PCM behavior. In the convection, the liquid goes up along the hot wall, then circulates horizontally along the cavity length. Raising the permeability in the direction along the flow improves the convection. When the large side of the AMFL is on the left, like in Figure 10, the impact of the AMFL is optimal. On the other hand, if its smaller size is on the left-hand side, the influence of the AMFL becomes limited. To address these aspects, the isotherms and MVF contours for all the considered configurations are depicted in Figure 11. Overall, the thermal distribution follows a similar

trend in all cases. Regarding the melting contours, it is clear that the remaining solid PCM is larger in configurations b and d compared with a and c, which is a further confirmation that melting is slower when the small part of the funnel-shaped AMFL is at the heated wall. It is important to note that anisotropic effects do not alter the total amount of MF but only modify its local properties. Consequently, the overall sensible heat capacity remains unchanged. However, because anisotropy influences local thermal conductivity and permeability, it can enhance heat transfer in certain geometric configurations. In this case, the variation in remaining solid PCM is attributed to differences in cumulative heat transfer rates throughout the melting process.

7 | Conclusions

In the present study, the impact of integrating a funnel-shaped AMFL in an LTHES storage compartment on the melting and energy storage of the PCM is examined. The compartment comprises a square cavity with a hot left wall, while the others are insulated. The equations governing the hydrothermal behavior of the PCM in the cavity are presented and solved using the FEM. Several configurations of the AMFL were tested by varying the percentage at which the AMFL covers the cavity from 36% to 60%, and by changing the geometrical orientation of the funnel shape by placing its larger side on the left or the right of the enclosure. The influence of these configurations on the melting duration and stored energy, as well as on the temperature distribution, was assessed. The results revealed that integrating the AMFL had an effect on the performance of the PCM. The importance of such an outcome stems from the fact that replacing an isotropic foam with an anisotropic one changes the orientation of the principal permeability without changing the overall porosity, that is, keeping the same amount of metallic matrix. It was further discovered that the arrangement of the AMFL geometry is significant. Orienting the broader end of the funnel shape toward the hot wall facilitates improved melting of the PCM due to the onset of heat transfer and convective flow in that region. Moving the longer size of the AMFL from the cold wall to the hot one raises the melting rate by 4.9%, 5.1%, and 3.9% when the AMFL covers 36%, 44%, and 52% of the cavity, respectively. Moreover, it was found that for the same geometry orientation, augmenting the AMFL size accelerates melting. Namely, it was found that raising the AMFL percentage from 36% to 60% increases the melting rate by 2.1% and 3.1% when the large size of the funnel is at the hot wall and the cold wall, respectively. Notably, it was also observed that the effect of the AMFL orientation is more significant than its scale. A smaller funnel-shaped AMFL with its large side at the hot wall is more effective than a larger AMFL with its large side at the cold wall. These findings indicate that the use of AMFL can be an efficient solution to improve the performance of porous PCM cavities without altering the solid metal content. Since the results indicate that the shape of AMFL affects the energy storage rate, testing a combination of vertically aligned AMFL along heated/cooled walls and horizontally aligned AMFL near insulated walls or dead zones could be beneficial. This arrangement would promote better flow in some areas while enhancing conduction effects in others.

Nomenclature

| | |
|------------------------|--|
| A_{mush} | mushy constant value, $10^{10} \text{ kg}/(\text{m}^3 \text{ s})$ |
| A_{sf} | interface surface between MF pore and HTF, $1/\text{m}$ |
| C_F | Frochheimer coefficient, m |
| d_{fp} | pore diameter, m |
| d_{fs} | pore characteristics, m |
| dV | volume element, m |
| e | porous structure constant, 0.339 |
| ES_{latent} | stored energy in the latent form, J |
| ES_{sensible} | stored energy in sensible form, J |
| g | gravity acceleration, m/s^2 |
| h_{sf} | interface heat transfer, $\text{W}/(\text{m} \cdot \text{K})$ |
| h_v | volumetric interface heat transfer, $\text{W}/(\text{m}^3 \cdot \text{K})$ |
| k | thermal conductivity, $\text{W}/(\text{m} \cdot \text{K})$ |
| Kn | anisotropy parameter |
| L | enclosure width, m |
| L_f | latent heat of fusion, J/kg |
| MVF | melted volume fraction |
| Nm | mesh control parameter |
| Pr | Prandtl number |
| Q_t | stored thermal energy, J/m |
| Re | Reynolds number |
| RRV_{MF} | HTF metal foam fill ratio |
| S_{MF} | distance between MF inserts in HTF, m |
| Symbol | unit, description |
| t | time, s |
| t | time, s |
| T_0 | reference temperature, K |
| T_{fu} | fusion temperature, K |
| T_h | hot temperature, K |
| t_{MF} | MFL thickness, m |
| u | r -velocity component, m/s |
| V | volume, m^3 |
| x, y | coordinate system, m |

Greek Symbols

| | |
|------------------------|---|
| α | thermal diffusivity, m^2/s |
| β | volume expansion, $1/\text{K}$ |
| ε | porosity |
| κ | porous permeability, m^2 |
| μ | dynamic viscosity, $\text{Pa} \cdot \text{s}$ |
| ω | anisotropy angle, $^\circ$ |
| ρ | density, kg/m^3 |
| σ | dummy parameter |
| γ_{mush} | mushy source term constant value, 0.001 |
| κ_{tor} | pore flow tortuosity |

μ_a artificial dynamic viscosity, 10^5 Pa·s
 $\varphi(T)$ melt fraction

Subscripts

AMFL anisotropic metal foam layer
 eff effective property
 HTF heat transfer fluid
 LHTES latent heat thermal energy storage
 MF metal foam
 PCM phase change materials
 PPI pore per inch

Acknowledgments

This work was supported and funded by the Deanship of Scientific Research at Imam Mohammad Ibn Saud Islamic University (IMSIU) (grant number IMSIU-DDRSP2503).

Data Availability Statement

The data that support the findings of this study are available from the corresponding author upon reasonable request.

References

1. M. Mofijur, T. Mahlia, A. Silitonga, et al., "Phase Change Materials (PCM) for Solar Energy Usages and Storage: An Overview," *Energies* 12 (2019): 3167.
2. D. Ghosh, J. Ghose, P. Datta, P. Kumari, and S. Paul, "Strategies for Phase Change Material Application in Latent Heat Thermal Energy Storage Enhancement: Status and Prospect," *Journal of Energy Storage* 53 (2022): 105179.
3. F. Hassan, F. Jamil, A. Hussain, et al., "Recent Advancements in Latent Heat Phase Change Materials and Their Applications for Thermal Energy Storage and Buildings: A State of the Art Review," *Sustainable Energy Technologies and Assessments* 49 (2022): 101646.
4. Y. Fang, J. Niu, and S. Deng, "Numerical Analysis for Maximizing Effective Energy Storage Capacity of Thermal Energy Storage Systems by Enhancing Heat Transfer in PCM," *Energy and Buildings* 160 (2018): 10–18.
5. C. Zhao, J. Wang, Y. Sun, S. He, and K. Hooman, "Fin Design Optimization to Enhance PCM Melting Rate Inside a Rectangular Enclosure," *Applied Energy* 321, no. C (2022): 119368.
6. S. Zhang, S. Mancin, and L. Pu, "A Review and Prospective of Fin Design to Improve Heat Transfer Performance of Latent Thermal Energy Storage," *Journal of Energy Storage* 62 (2023): 106825.
7. B. Lu, Y. Zhang, D. Sun, Z. Yuan, and S. Yang, "Experimental Investigation on Thermal Behavior of Paraffin in a Vertical Shell and Spiral Fin Tube Latent Heat Thermal Energy Storage Unit," *Applied Thermal Engineering* 187 (2021): 116575.
8. J. Wu, Q. Chen, Y. Zhang, and K. Sun, "Phase Change Material Heat Transfer Enhancement in Latent Heat Thermal Energy Storage Unit With Single Fin: Comprehensive Effect of Position and Length," *Journal of Energy Storage* 42 (2021): 103101.
9. Y. Tian, X. Liu, Q. Xu, et al., "Bionic Topology Optimization of Fins for Rapid Latent Heat Thermal Energy Storage," *Applied Thermal Engineering* 194 (2021): 117104.
10. S. Tiari, A. Hockins, and M. Mahdavi, "Numerical Study of a Latent Heat Thermal Energy Storage System Enhanced by Varying Fin Configurations," *Case Studies in Thermal Engineering* 25 (2021): 100999.
11. Y. Wu, J. Rong, D. Wang, et al., "Synergistic Enhancement of Heat Transfer and Thermal Storage Characteristics of Shell and Tube Heat Exchanger With Hybrid Nanoparticles for Solar Energy Utilization," *Journal of Cleaner Production* 387 (2023): 135882.
12. M. Abdolahimoghadam and M. Rahimi, "A Numerical Evaluation of a Latent Heat Thermal Energy Storage System in the Presence of Various Types of Nanoparticles," *Applied Thermal Engineering* 230 (2023): 120854.
13. F. Selimefendigil and C. Şirin, "Energy and Exergy Analysis of a Hybrid Photovoltaic/Thermal-Air Collector Modified With Nano-Enhanced Latent Heat Thermal Energy Storage Unit," *Journal of Energy Storage* 45 (2022): 103467.
14. S. Sami and N. Etesami, "Heat Transfer Enhancement of Micro-encapsulated Phase Change Material by Addition of Nanoparticles for a Latent Heat Thermal Energy Storage System," *Energy Reports* 7 (2021): 4930–4940.
15. S. K. Singh, S. K. Verma, and R. Kumar, "Thermal Performance and Behavior Analysis of SiO_2 , Al_2O_3 and MgO Based Nano-Enhanced Phase-Changing Materials, Latent Heat Thermal Energy Storage System," *Journal of Energy Storage* 48 (2022): 103977.
16. Y. Huo, M. Yin, and Z. Rao, "Heat Transfer Enhanced by Angle-Optimized Fan-Shaped Porous Medium in Phase Change Thermal Energy Storage System at Pore Scale," *International Journal of Thermal Sciences* 172 (2022): 107363.
17. M. T. Alam, A. Raj, L. K. Singh, and A. K. Gupta, "Configurational Assessment of Solidification Performance in a Triplex-Tube Heat Exchanger Filled With Composite Phase Change Material," *Applied Thermal Engineering* 230 (2023): 120814.
18. M. Thonon, G. Fraisse, L. Zalewski, and M. Pailha, "Simultaneous Charging and Discharging Processes in Latent Heat Thermal Energy Storage: A Review," *Thermal Science and Engineering Progress* 47 (2024): 102299.
19. J. M. Mahdi, S. Lohrasbi, and E. C. Nsofor, "Hybrid Heat Transfer Enhancement for Latent-Heat Thermal Energy Storage Systems: A Review," *International Journal of Heat and Mass Transfer* 137 (2019): 630–649.
20. A. Awasthi, K.-I. Hwang, and Y. Jeon, "Performance Improvement of Novel Latent Thermal Energy Storage System With Two-Layer Metal Foam Porosities," *Case Studies in Thermal Engineering* 60 (2024): 104668.
21. S. A. M. Mehryan, K. Ayoubi-Ayoubloo, M. Shahabadi, M. Ghalambaz, P. Talebizadehsardari, and A. Chamkha, "Conjugate Phase Change Heat Transfer in an Inclined Compound Cavity Partially Filled With a Porous Medium: A Deformed Mesh Approach," *Transport in Porous Media* 132, no. 3 (2020): 657–681.
22. M. Ghalambaz, K. Ayoubi Ayoubloo, and A. Hajjar, "Melting Heat Transfer of a Non-Newtonian Phase Change Material in a Cylindrical Vertical-Cavity Partially Filled Porous Media," *International Journal of Numerical Methods for Heat & Fluid Flow* 30, no. 7 (2020): 3765–3789.
23. A. NematpourKeshteli, M. Iasiello, G. Langella, and N. Bianco, "Using Metal Foam and Nanoparticle Additives With Different Fin Shapes for PCM-Based Thermal Storage in Flat Plate Solar Collectors," *Thermal Science and Engineering Progress* 52 (2024): 102690.
24. A. NematpourKeshteli, M. Iasiello, G. Langella, and N. Bianco, "Optimization of the Thermal Performance of a Lobed Triplex-Tube Solar Thermal Storage System Equipped With a Phase Change Material," *Heliyon* 10, no. 16 (2024): e36105.
25. M. T. Alam, R. Kumar, and A. K. Gupta, "Optimizing Diverse Triplex-Tube Heat Storage Systems With Composite Phase Change Materials in Simultaneous Charging and Discharging Environment," *International Communications in Heat and Mass Transfer* 155 (2024): 107478.
26. L. J. Gibson, "Cellular Solids," *MRS Bulletin* 28, no. 4 (2003): 270–274.
27. S. Liu, H. Wang, Q. Ying, and L. Guo, "Numerical Study on the Combined Application of Multiple Phase Change Materials and

- Gradient Metal Foam in Thermal Energy Storage Device,” *Applied Thermal Engineering* 257 (2024): 124267.
28. V. Joshi and M. K. Rathod, “Thermal Transport Augmentation in Latent Heat Thermal Energy Storage System by Partially Filled Metal Foam: A Novel Configuration,” *Journal of Energy Storage* 22 (2019): 270–282.
29. V. Joshi and M. K. Rathod, “Constructal Enhancement of Thermal Transport in Metal Foam-PCM Composite-Assisted Latent Heat Thermal Energy Storage System,” *Numerical Heat Transfer, Part A: Applications* 75, no. 6 (2019): 413–433.
30. M. Mozaffari, A. Hajjar, M. Sheremet, O. Younis, and M. Ghalambaz, “Enhancing LHTES Efficiency Using Asymmetric Hexagon Anisotropic Metal Foam Layer: A Comparative Study on Orientation and Scale,” *Thermal Science and Engineering Progress* 59 (2025): 103343.
31. B. Buonomo, D. Ercole, O. Manca, and S. Nardini, “Numerical Analysis on a Latent Thermal Energy Storage System With Phase Change Materials and Aluminum Foam,” *Heat Transfer Engineering* 41, no. 12 (2020): 1075–1084.
32. M. Ghalambaz, S. A. M. Mehryan, K. A. Ayoubloo, et al., “Thermal Energy Storage and Heat Transfer of Nano-Enhanced Phase Change Material (NePCM) in a Shell and Tube Thermal Energy Storage (TES) Unit With a Partial Layer of Eccentric Copper Foam,” *Molecules* 26 (2021): 1491.
33. M. Falcone, D. Rehman, M. Dongellini, C. Naldi, B. Pulvirenti, and G. L. Morini, “Experimental Investigation on Latent Thermal Energy Storages (LTESs) Based on Pure and Copper-Foam-Loaded PCMs,” *Energies* 15 (2022): 4894.
34. V. Joshi and M. K. Rathod, “Experimental and Numerical Assessments of Thermal Transport in Fins and Metal Foam Infused Latent Heat Thermal Energy Storage Systems: A Comparative Evaluation,” *Applied Thermal Engineering* 178 (2020): 115518.
35. M. Esmaeili Shayan, G. Najafi, and G. Lorenzini, “Phase Change Material Mixed With Chloride Salt Graphite Foam Infiltration for Latent Heat Storage Applications at Higher Temperatures and Pressures,” *International Journal of Energy and Environmental Engineering* 13, no. 2 (2022): 739–749.
36. G. Shu, T. Xiao, J. Guo, P. Wei, X. Yang, and Y.-L. He, “Effect of Charging/Discharging Temperatures Upon Melting and Solidification of PCM-Metal Foam Composite in a Heat Storage Tube,” *International Journal of Heat and Mass Transfer* 201 (2023): 123555.
37. S. M. Hashem Zadeh, M. Ghodrat, K. Ayoubi Ayoubloo, N. Sedaghatizadeh, and R. A. Taylor, “Partial Charging/Discharging of Bio-Based Latent Heat Energy Storage Enhanced With Metal Foam Sheets,” *International Communications in Heat and Mass Transfer* 130 (2022): 105757.
38. M. Yang, M. A. Moghimi, R. Loillier, C. N. Markides, and M. Kadivar, “Design of a Latent Heat Thermal Energy Storage System Under Simultaneous Charging and Discharging for Solar Domestic Hot Water Applications,” *Applied Energy* 336 (2023): 120848.
39. Y. Mase, Z. F. Sucipto, and M. Mobedi, “A Numerical Study on Control Mechanism of Heat Transfer in a Double Pipe PCM Heat Exchanger by Changing Eccentricity,” *Energy* 291 (2024): 130266.
40. L. Liang, Y. H. Diao, Y. H. Zhao, Z. Y. Wang, and C. Q. Chen, “Experimental and Numerical Investigations of Latent Thermal Energy Storage Using Combined Flat Micro-Heat Pipe Array-Metal Foam Configuration: Simultaneous Charging and Discharging,” *Renewable Energy* 171 (2021): 416–430.
41. E. Wang, C. Chen, G. Zhang, Q. Luo, Q. Li, and G. Sun, “Multiaxial Mechanical Characterization of Additively Manufactured Open-Cell Kelvin Foams,” *Composite Structures* 305 (2023): 116505.
42. M. Zafari, M. Panjepour, M. Davazdah Emami, and M. Meratian, “Microtomography-Based Numerical Simulation of Fluid Flow and Heat Transfer in Open Cell Metal Foams,” *Applied Thermal Engineering* 80 (2015): 347–354.
43. M. Iasiello, N. Bianco, W. Chiu, and V. Naso, “Anisotropy Effects on Convective Heat Transfer and Pressure Drop in Kelvin's Open-Cell Foams,” *Journal of Physics: Conference Series* 923 (2017): 012035.
44. S. Zhang, Y. Yao, Y. Jin, Z. Shang, and Y. Yan, “Heat Transfer Characteristics of Ceramic Foam/Molten Salt Composite Phase Change Material (CPCM) for Medium-Temperature Thermal Energy Storage,” *International Journal of Heat and Mass Transfer* 196 (2022): 123262.
45. M. Ghalambaz, A. A. Melaibari, A. J. Chamkha, O. Younis, and M. Sheremet, “Phase Change Heat Transfer and Energy Storage in a Wavy-Tube Thermal Storage Unit Filled With a Nano-Enhanced Phase Change Material and Metal Foams,” *Journal of Energy Storage* 54 (2022): 105277.
46. D. A. Nield and A. Bejan, *Convection in Porous Media* (Springer, 2006).
47. Y. Yao and H. Wu, “Interfacial Heat Transfer in Metal Foam Porous Media (MFPM) Under Steady Thermal Conduction Condition and Extension of Lemlich Foam Conductivity Theory,” *International Journal of Heat and Mass Transfer* 169 (2021): 120974.
48. M. Iasiello, N. Bianco, W. K. S. Chiu, and V. Naso, “Anisotropic Convective Heat Transfer in Open-Cell Metal Foams: Assessment and Correlations,” *International Journal of Heat and Mass Transfer* 154 (2020): 119682.
49. M. Ghalambaz, M. Sheremet, K. Shank, S. Tiari, and M. Fteiti, “Improving Phase Change Heat Transfer in an Enclosure Partially Filled by Uniform and Anisotropic Metal Foam Layers,” *International Journal of Heat and Mass Transfer* 228 (2024): 125678.
50. M. Ghalambaz, M. Aljaghtham, A. J. Chamkha, A. Abdullah, A. Alshehri, and M. Ghalambaz, “An Anisotropic Metal Foam Design for Improved Latent Heat Thermal Energy Storage in a Tilted Enclosure,” *International Journal of Mechanical Sciences* 238 (2022): 107830.
51. A. I. N. Korti and H. Guellil, “Experimental Study of the Effect of Inclination Angle on the Paraffin Melting Process in a Square Cavity,” *Journal of Energy Storage* 32 (2020): 101726.
52. A. Agarwal and R. Sarviya, “Characterization of Commercial Grade Paraffin Wax as Latent Heat Storage Material for Solar Dryers,” *Materials Today: Proceedings* 4, no. 2 (2017): 779–789.
53. N. Ukrainczyk, S. Kurajica, and J. Šipušić, “Thermophysical Comparison of Five Commercial Paraffin Waxes as Latent Heat Storage Materials,” *Chemical and Biochemical Engineering Quarterly* 24, no. 2 (2010): 129–137.
54. Y. Yao and H. Wu, “Macroscale Modeling of Solid-Liquid Phase Change in Metal Foam/Paraffin Composite: Effects of Paraffin Density Treatment, Thermal Dispersion, and Interstitial Heat Transfer,” *Journal of Thermal Science and Engineering Applications* 13, no. 4 (2021): 041024.
55. N. B. Khedher, M. Sheremet, A. M. Hussin, S. A. M. Mehryan, and M. Ghalambaz, “The Effect of Hot Wall Configuration on Melting Flow of Nano-Enhanced Phase Change Material Inside a Tilted Square Capsule,” *Journal of Energy Storage* 69 (2023): 107921.
56. H. Zheng, C. Wang, Q. Liu, Z. Tian, and X. Fan, “Thermal Performance of Copper Foam/Paraffin Composite Phase Change Material,” *Energy Conversion and Management* 157 (2018): 372–381.